

Cite this: DOI: 00.0000/xxxxxxxxxx

# Janus MoS<sub>2</sub>/WS<sub>2</sub> Heterobilayers as Selective Photocatalysts for Water Splitting<sup>†</sup>

Mostafa Torkashvand<sup>✉<sup>a,b</sup></sup>, Saeedeh Sarabadani Tafreshi<sup>✉<sup>a</sup></sup>, Caterina Cocchi<sup>✉<sup>b</sup></sup>, and Surender Kumar<sup>✉<sup>b</sup></sup>

Received Date

Accepted Date

DOI: 00.0000/xxxxxxxxxx

Identifying materials that simultaneously straddle the water redox potentials and possess an intrinsic electric field is crucial for achieving high solar-to-hydrogen (STH) efficiency. Using state-of-the-art first-principles calculations, including a range-separated hybrid functional and spin-orbit coupling, we investigate MoXY/WXY (X, Y = S, Se) Janus bilayers for overall water splitting. We find that the Se–Se interfaced heterobilayer is intrinsically capable of driving water splitting, while its S–S counterpart can meet the redox requirements through pH modulation. For both configurations, a remarkable STH efficiency of 17.1% is predicted. Compared with homo-bilayers, hetero-bilayers benefit from the chemical potential difference between Mo and W, which generates a built-in electric field and promotes spatial separation of photogenerated carriers, suppressing recombination and overall enhancing hydrogen production. These results demonstrate the promise of Janus heterobilayers for efficient solar-driven water splitting.

## Introduction

Photocatalytic water splitting is regarded as a promising carbon-neutral route for hydrogen production through the direct conversion of solar energy into chemical fuel.<sup>1–5</sup> Given the global abundance of solar energy and water, hydrogen generation via photocatalytic water splitting is highly sustainable, environmentally friendly, and potentially cost-effective.<sup>3,4,6</sup> The underlying mechanism for photocatalytic water splitting begins with the excitation of the photocatalyst, which generates electron–hole pairs upon photo-absorption. The generated charge carriers play a central role in redox reactions, and their rapid separation and transport are essential to suppress charge recombination promoted by Coulomb attraction.<sup>4,7</sup>

An effective photocatalyst for water splitting should have a conduction band minimum (CBM) higher than the reduction potential (-4.44 eV for  $H^+/H_2$  relative to vacuum) and the valence band maximum (VBM) lower than the oxidation potential (-5.67 eV for  $O_2/H_2O$ ).<sup>2–4,7,8</sup> Moreover, a band gap exceeding the thermodynamic threshold of 1.23 eV is necessary for maximizing the solar-to-hydrogen (STH) efficiency.<sup>2,3,9–12</sup> While redox ability requires a large band gap, visible light-harvesting is optimized by a fundamental gap energy falling in the visible region. These two con-

ditions, which are crucial for high efficiency,<sup>9</sup> are challenging to achieve simultaneously and demand the design of novel materials.

In the last decade, two-dimensional (2D) transition metal dichalcogenides (TMDs) have emerged as key materials in photocatalytic research.<sup>6,8,10–17</sup> These systems are uniquely suited for solar-driven water splitting due to their robust chemical stability, band gaps within the visible spectrum, and exceptional structural tunability.<sup>8,10–13,15,17,18</sup> TMDs offer a large compositional and structural versatility, including from pristine monolayers to asymmetric Janus structures and complex van der Waals (vdW) heterostructures.<sup>8–13,15,17–19</sup> This diversity allows a precise control over electronic properties through thickness modulation and tailored stacking,<sup>8,10–13,15,17,18</sup> maximizing light harvesting and enhancing charge carrier separation, which are the fundamental requirements for high-performance photocatalysis.

Due to their broken out-of-plane structural symmetry, Janus TMDs have recently emerged as a particularly promising material platform for photocatalysis.<sup>8,10–13,15,17,18</sup> By substituting one layer of chalcogen atoms with another species in the same group (e.g., S → Se)<sup>20,21</sup>, a static dipole moment is generated perpendicular to the basal plane, giving rise to a permanent internal polarization that is absent in conventional, symmetric monolayers.<sup>8–12,15,17–19</sup> This built-in electric field can act as an intrinsic driving force for water splitting by producing a continuous potential gradient that effectively separates photo-generated charge carriers. While monolayers and homo-metal Janus bilayers have been largely investigated to achieve tunable band align-

<sup>a</sup> Department of Chemistry, Amirkabir University of Technology, 1591634311 Tehran, Iran; E-mail: s.s.tafreshi@aut.ac.ir

<sup>b</sup> Institut für Festkörpertheorie und -Optik, Friedrich-Schiller-Universität Jena, 07743 Jena, Germany, E-mail: caterina.cocchi@uni-jena.de, surendermohinder@gmail.com

<sup>†</sup> Supplementary Information available: [details of any supplementary information available should be included here]. See DOI: 00.0000/00000000.

ment and enhanced carrier lifetimes,<sup>8,10-13,15,17,18</sup> TMD Janus heterobilayers remain largely unexplored.

Including different transition metals,<sup>19,22</sup> TMD Janus heterobilayers introduce a reciprocity between layer-specific dipoles and a metal-to-metal chemical potential difference that further enhance and modulate the built-in electric field,<sup>9,19</sup> promoting the selective hydrogen and oxygen evolution reactions on distinct surfaces. Moreover, the directionality of the intrinsic dipoles can lead to distinct migration pathways for photogenerated carriers,<sup>7</sup> whereby appropriate stacking order may additionally suppress interfacial charge recombination, maximizing carrier utilization efficiency and ultimately leading to superior STH conversion yield.

Here, we investigate from first principles the electronic structure and photocatalytic ability of TMD Janus heterobilayers with chemical formula  $\text{MoXY/WXY}$  (where  $X, Y \in \{\text{S}, \text{Se}\}$ ). By exploring four configurations with AB-stacking and comparing them against their homo-metal counterparts, we establish clear trends regarding the influence of metal-to-metal chemical potential differences and stacking order on the built-in electric field. Our analysis of band offsets and pH-dependent redox potentials identifies two specific configurations that are capable of spontaneous overall water splitting. The stacking-dependent work function dictates the optimal operational environment: the bilayer with the highest work function is optimized for acidic conditions ( $\text{pH} = 0$ ), while the lowest work function imposes alkaline conditions ( $\text{pH} = 12.5$ ) to align with the Nernstian-shifted redox levels. For these systems, we obtain a remarkable STH efficiency of 17.14%. Other bilayers show selective catalytic behavior, limited to either the oxygen evolution reaction (OER) or the hydrogen evolution reaction (HER).

## Computational details

We performed density-functional theory (DFT) calculations with the projector augmented wave (PAW) method for electron-ion interaction, as implemented in the Vienna Ab initio Simulation Package (VASP).<sup>23-26</sup> The exchange-correlation functional is treated within the generalized gradient approximation of Perdew, Burke, and Ernzerhof (PBE)<sup>27</sup> during relaxation, while the Heyd-Scuseria-Ernzerhof (HSE06) screened hybrid functional<sup>28,29</sup> is adopted to compute the electronic and photocatalytic properties. Structural optimization is conducted until the total energy is below  $10^{-6}$  eV and the Hellmann-Feynman forces are less than 0.01 eV/Å per atom. To account for long-range dispersion forces, the DFT-D3 semi-empirical correction is applied.<sup>30,31</sup> A plane-wave basis set with a kinetic energy cutoff of 550 eV and a  $\Gamma$ -centered  $15 \times 15 \times 1$   $\mathbf{k}$ -point grid is used for all systems. In the HSE06 calculations, the total-energy convergence threshold is reduced to  $10^{-5}$  eV. A vacuum layer exceeding 20 Å is included along the  $z$ -direction to eliminate spurious interactions between periodic images. Given the broken inversion symmetry and intrinsic polarity of the Janus layers, a dipole correction is included to ensure an accurate alignment to the vacuum level. Spin-orbit coupling (SOC) is included in the electronic property calculations. The post-processing analysis is done with the VASPKIT<sup>32</sup> tool and in-house-produced Python scripts.

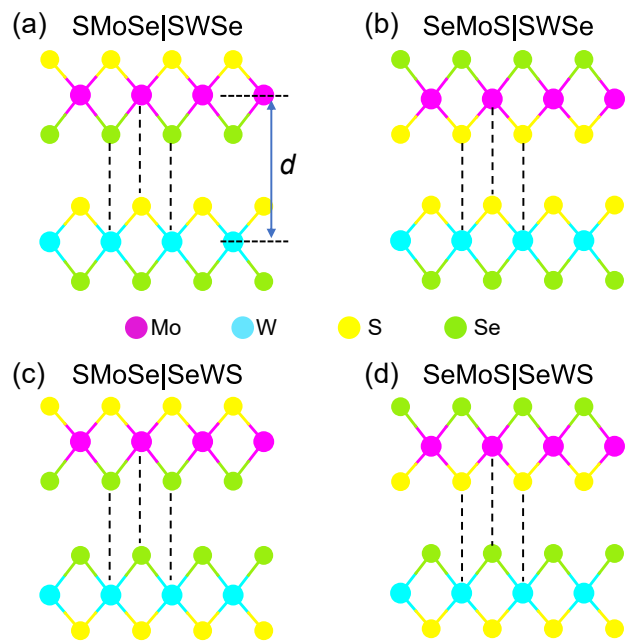


Fig. 1 Side views of the optimized AB-stacked MoSSe/WSSe heterobilayers in the 2H phase: (a) SMoSe|SWSe, (b) SeMoS|SWSe, (c) SMoSe|SeWS, and (d) SeMoS|SeWS. The blue arrow in panel (a) indicates the metal–metal distance  $d$ . The gray dashed bars guide the eyes to recognize the stacking configuration.

## Results and discussion

### Structural properties

We investigate four AB-stacked configurations of TMD Janus heterobilayers composed of MoSSe and WSSe.<sup>22</sup> These systems are categorized by their chalcogen interfaces,<sup>22,33</sup> with either the same species (S|S or Se|Se) or different species (S|Se or Se|S) facing each other (Fig. 1). In the considered AB-stacking, the metal atom in one Janus monolayer aligns vertically with a chalcogen atom in the other monolayer. To avoid the lattice mismatch that naturally emerge from the difference in the in-plane lattice constants of the two monolayers, ranging between 3.16 Å<sup>34-37</sup> to 3.29 Å<sup>8,37-39</sup> in the Mo- and W-based sheets, respectively, we assign to all configurations an initial lattice constant of  $a = 3.29$  Å. Upon structural optimization, all heterobilayers maintain the same value of  $a = 3.23$  Å, which, however, substantially reduces compared to the input value, effectively averaging the lattice constants of the single constituents (Table 1). This results in inherent strain that, combined with the broken mirror symmetry of the Janus monolayers, uniquely defines the structural properties of these heterostructures.

The metal-chalcogen bond lengths are nearly identical in all considered systems, in agreement with previous theoretical and experimental reports.<sup>19,22,33,40</sup> In contrast, the interlayer distance  $d$ , defined as the metal–metal separation along the out-of-plane direction, shows a strong dependence on the chalcogen interface (Table 1). Specifically, Se|Se interfaced bilayers display the largest interlayer distance  $d = 6.88$  Å, whereas those with an S|S interface show the smallest separation ( $d = 6.40$  Å). For

Table 1 Structural properties of hetero metal bilayers: Lattice constants (a), metal-metal distance (d), various metal-chalcogenide bond-lengths and binding energies ( $E_b$ ).

Configuration	$a$ (Å)	$d$ (Å)	$d_{\text{Mo-S}}$ (Å)	$d_{\text{Mo-Se}}$ (Å)	$d_{\text{W-S}}$ (Å)	$d_{\text{W-Se}}$ (Å)	$E_b$ (eV)
SMoSe SWSe	3.23	6.62	2.413	2.53	2.42	2.53	-2.23
SeMoS SWSe	3.23	6.40	2.410	2.53	2.42	2.53	-2.21
SMoSe SeWS	3.23	6.89	2.412	2.53	2.42	2.53	-2.24
SeMoS SeWS	3.23	6.62	2.411	2.53	2.42	2.53	-2.22

mixed S|Se interfaces, the interlayer distance adopts an intermediate value of 6.62 Å, approximately equal to the average of the other two.<sup>33,40</sup>

The relative stability of the heterostructures is estimated by their binding energy, defined as

$$E_b = E_{\text{hetero}} - E_{\text{MoSSe}} - E_{\text{WSSe}}, \quad (1)$$

where  $E_{\text{hetero}}$ ,  $E_{\text{MoSSe}}$ , and  $E_{\text{WSSe}}$  are the DFT total energies of the hetero-bilayers and their isolated monolayer constituents, respectively. All calculated binding energies are negative [Table 1, for homo-metals see the Electronic Supplementary Information (ESI), Table S1], confirming energetic stability, and range between -2.24 eV in SMoSe|SeWS to -2.21 eV in SeMoS|SWSe.

## Electronic properties

The considered Janus hetero-bilayers show distinct electronic band structures (Fig. 2(a)). Except for the SeMoS|SeWS heterostructure, which exhibits a direct band gap at the high-symmetry point K, the other systems are characterized by an indirect band gap. In the SMoSe|SWSe bilayer, featuring a fundamental gap of 1.61 eV (Table 2), the VBM at  $\Gamma$  is primarily localized on the MoSSe layer, while the CBM, exhibiting signatures of interlayer hybridization via mixed orbital contributions, appears between K and  $\Gamma$ , at the so-called Q-valley.<sup>33</sup> Conversely, in the SeMoS|SWSe bilayer, the VBM remains at  $\Gamma$  while the CBM appears at the K-point, leading to an indirect gap of 1.43 eV. Here, the layer contributions are reversed compared to SMoSe|SWSe, with the VBM arising from WSSe and the CBM from MoSSe. In SMoSe|SeWS, the uppermost valence band at K is above the  $\Gamma$ -valley, while the lowest CB at Q remains below the K-point, leading to an indirect gap of 1.56 eV with VBM and CBM localized on the WSSe and MoSSe monolayers, respectively. Finally, the SeMoS|SeWS bilayer has a direct band gap of 1.00 eV at the K-valley. Remarkably, in all these AB-stacked Janus heterostructures, the frontier bands remain mostly localized on a specific monolayer, indicating suppressed hybridization.

The analysis of the projected density of states (PDOS) (Fig. 2(b)) reveals the atomic contributions to the electronic structure of the considered hetero-bilayers. As expected,<sup>13,40–42</sup> the band edges are dominated by contributions from the transition-metal species, Mo and W, which strongly influence the overall shape of the PDOS and allow retrieving the trends identified in Fig. 2(a), particularly the type-II level alignment. While this characteristic is common to all heterobilayers, the spatial localization of the VBM and CBM is sensitive to the composition. In

SMoSe|SWSe, the VBM is localized on the Mo-containing monolayer and the CBM on the W-based one, whereas the opposite is true in all other systems.

We deepen the electronic-structure analysis by inspecting in detail the effects of spin-polarization and SOC, highlighted in the spin-projected band structures presented in Fig. 3. In the SMoSe|SWSe bilayer, the CBM at the Q-valley shows a significant spin splitting, whereas the VBM splitting at the K-point remains small. This is consistent with the characteristics of the constituents: the CBM is primarily dominated by the heavy W atoms in the WSSe layer, which possess a larger atomic SOC constant, while the VBM is stems from Mo states in the MoSSe monolayer. A similar behavior is observed across other configurations, where bands associated with the WSSe monolayer shows larger spin-splitting values ( $\sim 600$  meV) compared to those localized in MoSSe. The large spin-orbit splitting affecting the WSSe monolayers render the band-gap nature of SeMoS|SeWS particularly sensitive to relativistic effects: without SOC, this system features an indirect band gap, as predicted in previous reports<sup>22</sup>. In fact, ignoring SOC, the VBM at the K-valley resides slightly lower than the  $\Gamma$ -point, while when SOC is included, the VBM shifts to the zone center, although the energies at these two high-symmetry points remain very close. Another important characteristic of these Janus heterobilayers emerging from Fig. 3 is the spin-polarization of the band edges. While in SeMoS|SWSe, SMoSe|SeWS, and SeMoS|SeWS the highest-occupied and lowest-unoccupied states at the K-valley have parallel spins, in SMoSe|SWSe, both the CBM at Q and the lowest-energy conduction state at K have spin-up while the uppermost valence band has spin-down. This feature is expected to impact the optical absorption of these hetero-bilayers. An in-depth analysis on this behavior will be the subject of up-coming work.

The presence of different chalcogen species in the Janus structures creates a built-in electric field within each monolayer.<sup>13,14,42,43</sup> When these monolayers are combined to form a hetero-bilayers, the intrinsic dipoles of the constituents generate an interfacial electrostatic potential which is further modulated by the mutual orientation of the monolayers (Fig. 4). The varying depth of the electrostatic potential arises precisely from the different electronegativity and size of the atoms, being therefore maximized in WSSe. The orientation of the generated field is determined by the chalcogen arrangement, expectedly pointing from Se to S, namely from the more positively to the more negatively charged regions.

In the SMoSe|SWSe and SeMoS|SeWS configurations, the intrinsic dipole moments of the monolayers point to the same direc-

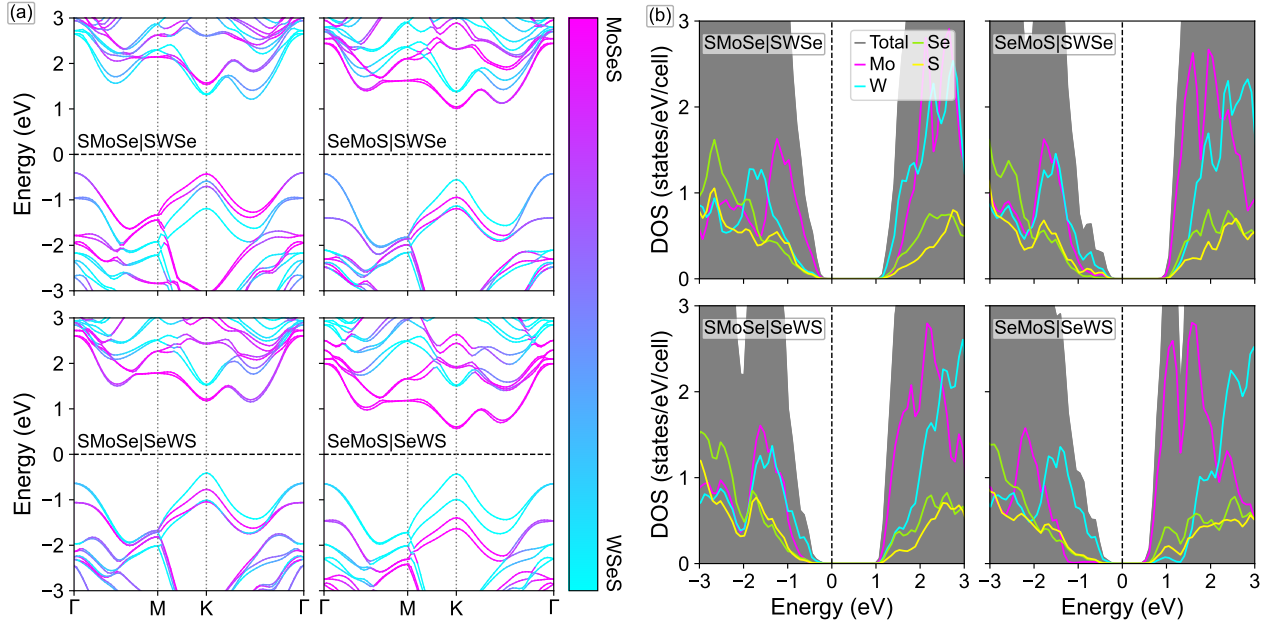


Fig. 2 (a) Layer-projected electronic band structures of the considered Janus hetero-bilayers calculated using the HSE06 hybrid functional with spin-orbit coupling. (b) Total (gray area) and atom-projected density of states. In all graphs, the Fermi level is set to 0 eV.

Table 2 Calculated band gaps from HSE06 ( $E_g^{\text{HSE06}}$ ) with the direct one obtained for SeMoS|SeWS bolded, dipole moments ( $\mu$ ), electrostatic potential difference ( $\Delta\Phi$ ) within the hetero-bilayers, and work function ( $W$ ).

Configuration	$E_g^{\text{HSE06}}$ (eV)	$\mu$ (D)	$\Delta\Phi$ (eV)	$W$ (eV)
SMoSe SWSe	1.61	0.346	1.32	5.72
SeMoS SWSe	1.43	0.002	0.18	4.60
SMoSe SeWS	1.56	0.017	0.18	5.51
SeMoS SeWS	<b>1.00</b>	-0.321	1.09	5.30

tion, resulting in a strong additive effect. This leads to substantial potential differences of 1.32 eV and 1.25 eV, respectively, and to total dipole moments up to 0.345 D (Table 2). For the remaining two configurations, the monolayers are oriented with opposing internal fields that nearly cancel each other out, resulting in a negligible net electric field and negligible dipole moments equal or below 0.02 D. This dramatic difference in the internal field strength directly influences the band alignment and the spatial separation of charge carriers across the interface.

The work functions of the hetero-bilayers, computed from the difference between the vacuum level and the Fermi energy (Table 2), provide another relevant indicator regarding the potential performance of these systems in photocatalysis. The SeMoS|SWSe bilayer exhibits the lowest work function (4.60 eV), whereas SMoSe|SWSe shows the highest value (5.72 eV). This large variation originates from interface-dependent charge redistribution and the resulting dipole-induced shift of the vacuum level. Such work-function differences directly determine the absolute band-edge alignment with aqueous redox potentials, thereby governing carrier transfer at the semiconductor–electrolyte interface and, consequently, the efficiency of photocatalytic water splitting, as discussed below.

## Photocatalytic properties

With the detailed knowledge of the electronic structure of the TMD Janus hetero-bilayers, we now evaluate their performance in photocatalytic water splitting by comparing their band edges with the water redox potentials. We recall that the overall water-splitting mechanism includes both the OER<sup>8,9,15,19</sup>,  $4h^+ + 2H_2O \rightarrow O_2 + 4H^+$  and the HER,  $4e^- + 4H_2O \rightarrow 2H_2 + 4OH^-$ . In this process, photoexcited electrons are transferred from the CBM of the catalyst to drive the reduction process, while photogenerated holes at the VBM facilitate the oxidation process. Consequently, the thermodynamic feasibility of these reactions heavily depends on the absolute values of the CBM and VBM relative to the standard reduction potential of  $H^+/H_2$  at 4.44 eV and the oxidation potential of  $H_2O/O_2$  at -5.67 eV (pH=0). Beyond the requirement that the band edges straddle the redox potentials, the kinetic overpotentials, namely the energy difference between the band edges and the redox levels, should be large enough to overcome the activation barriers of each half-reaction.

An overview of the frontier energy levels of the considered Janus hetero-bilayers relative to the redox potential, compared for reference with the same results computed for the homo-bilayers, is reported in Fig. 5. Similar to the homo-bilayers featuring a Se-Se interface (SMoSe|SeMoS and SWSe|SeWS), which are

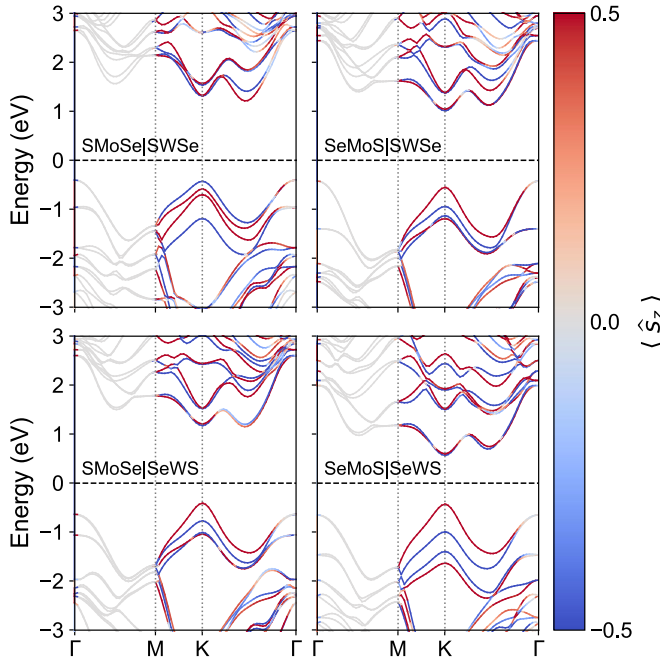


Fig. 3 Spin-projected electronic band structures ( $s_z$  component) of the Janus heterobilayer configurations, calculated at the HSE06+SOC level of theory. The bands are color-coded based on their  $s_z$  spin expectation values to visualize spin-splitting and potential Rashba-like features. In all panels, the Fermi level ( $E_F$ ) is shifted to 0 eV, indicated by horizontal dashed line.

the only ones fulfilling the requirement for overall catalytic water splitting at pH= 0,<sup>13–15,19,44</sup> among the hetero-bilayers, only SMoSe|SeWS exhibits the desired band alignment. In this system, the CBM is 80 meV above the  $H_2$  reduction level, and the VBM is 250 meV below the oxygen reduction threshold, demonstrating the catalytic robustness of this heterostructure.

The remaining three hetero-bilayers fulfill only one condition at pH= 0. In SMoSe|SWSe, the CBM lies approximately 100 meV below the  $H_2$  reduction level, rendering it incapable of hydrogen evolution, although its VBM is positioned deep enough to effectively oxidize  $O_2$ . Conversely, in SeMoS|SWSe, the VBM is over 500 meV above the  $O_2$  redox level, making it unsuitable for oxygen evolution, even though the CBM is well-positioned for  $H_2$  reduction. The SeMoS|SeWS configuration lacks the necessary band gap threshold of 1.23 eV. Moreover, while its VBM lies slightly below the  $O_2$  redox level, its CBM is significantly below the  $H_2$  level, preventing the HER.

The results presented in Fig. 5 suggest that the Se-Se interface is a crucial requirement for Janus bilayers to operate as effective photocatalysts at pH= 0. However, the different chemical potentials (or electronegativities) of the metal atoms in the hetero-bilayers lead to the formation of a permanent dipole moment, which represents a strategic advantage compared to the homo-bilayers, where the internal fields from each layer cancel out completely. As shown schematically in Fig. 5 (left), the MoSSe monolayer has a slightly more positive charge than WSSe, as expected from the deeper electrostatic potential of W compared to Mo (compare Fig. 4). This imbalance creates an internal electric

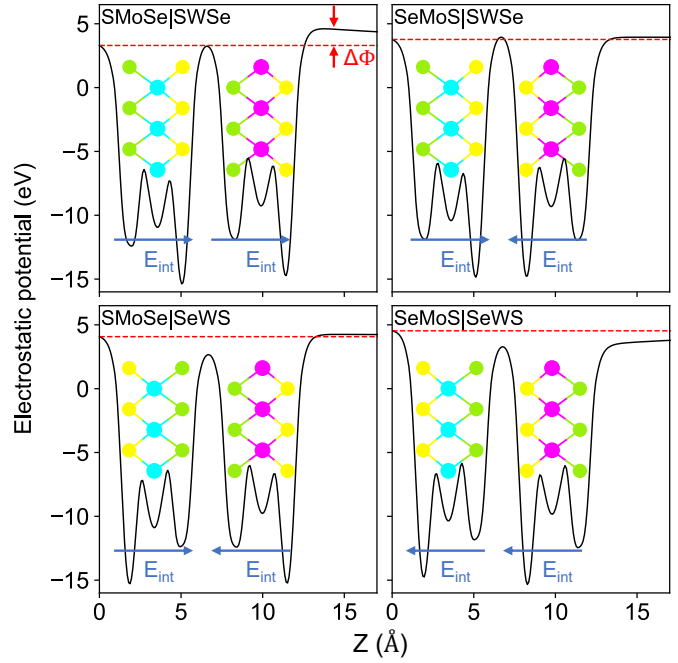


Fig. 4 One-dimensional profile of the planar-averaged Hartree potential for various heterobilayers. Red arrows denote the potential difference ( $\Delta\Phi$ ) between the two surfaces of the bilayer, while blue arrows indicate the intrinsic internal electric field within each Janus monolayer.

field directed from the MoSSe toward the WSSe layer. Because the CBM of MoSSe is lower than that of WSSe, this built-in electric field facilitates the migration of electrons from WSSe to MoSSe. Concomitantly, the higher VBM in WSSe compared to MoSSe allows the former to accept holes from the latter, a process that would be inhibited in the absence of an electric field.

Based on these considerations, the intrinsic dipole moment of the Janus hetero-bilayers is expected to promote the spatial separation of photogenerated electrons and holes into different layers. By physically isolating charge carriers of opposite sign, the exciton recombination rate is likely reduced, allowing efficient water splitting, particularly in the SMoSe|SeWS.

#### Photocatalytic Performance Modulation

The efficiency of photocatalytic water splitting is intimately linked to the pH of the aqueous environment, which controls the positions of the water redox potentials. The pH-dependent redox potentials at room temperature are governed by the Nernst equation<sup>19,45–47</sup>:  $E_{pH} = E_{pH=0} - 0.059 \cdot pH$  where  $E_{pH}$  is the redox potential at a specific acidity or alkalinity level. As the pH value increases from 0 to 14, the redox potentials for both HER and OER shift upward in energy.

To account for pH variations depending on the catalytic environment, we reassess the alignment of the frontier levels of the considered hetero-bilayers (and homo-bilayers for reference) with respect to the modified values of the HER and OER potentials at pH= 7 and pH= 14 (Figure 5). At pH= 7 (neutral environment), none of the considered systems fulfill the conditions for HER and OER simultaneously. On the other hand, at extreme alkaline conditions (pH= 14), both the SeWS|SeWS homo-

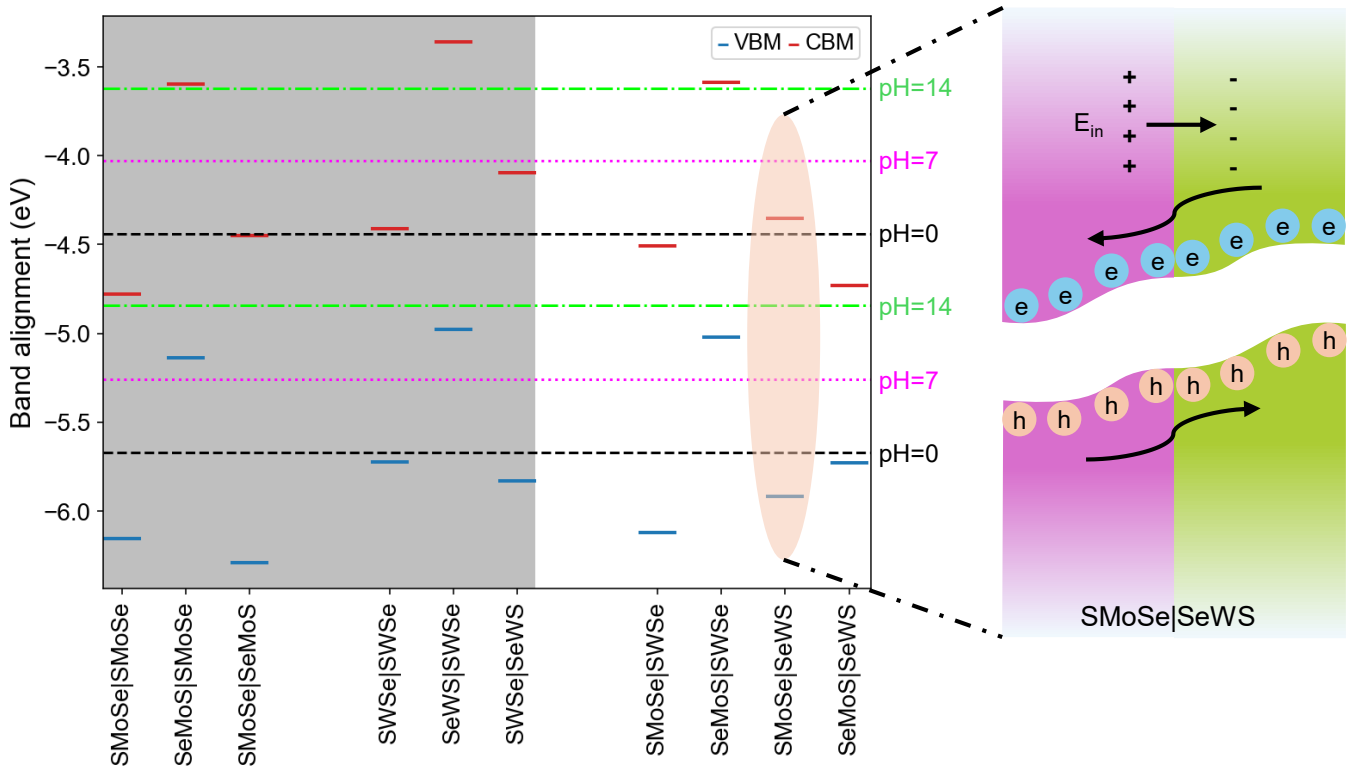


Fig. 5 Band alignment of homo-metal (gray background) and hetero-metal Janus bilayers relative to the water redox potentials referenced to the vacuum level set to 0 eV. The scheme on the right illustrates the band offsets and the direction of the built-in electric field in the SeMoS|SeWS heterobilayer.

bilayer and the SeMoS|SWSe hetero-bilayer, which are inactive at lower pH values, become capable of overall water splitting in the range  $11.5 \leq \text{pH} \leq 14$ , as their band edges successfully straddle the shifted redox levels.

The overall water splitting ability of a catalyst is quantified by its STH efficiency ( $\eta_{\text{STH}}$ ),<sup>8,9,19</sup> defined as the product of the light absorption efficiency ( $\eta_{\text{abs}}$ ) and the carrier utilization efficiency ( $\eta_{\text{cu}}$ )<sup>8,9,15,19</sup>:

$$\eta_{\text{STH}} = \eta_{\text{abs}} \cdot \eta_{\text{cu}}. \quad (2)$$

The light absorption efficiency represents the fraction of the total incident solar power that the semiconductor can potentially absorb, determined by its band gap and the standard solar flux spectrum,  $P(\hbar\omega)$ :

$$\eta_{\text{abs}} = \frac{\int_{E_g}^{\infty} P(\hbar\omega) d(\hbar\omega)}{\int_0^{\infty} P(\hbar\omega) d(\hbar\omega)}. \quad (3)$$

The carrier utilization efficiency is the ratio of the generated chemical energy to the total absorbed solar power, calculated as:

$$\eta_{\text{cu}} = \frac{\Delta G \int_E^{\infty} \frac{P(\hbar\omega)}{\hbar\omega} d(\hbar\omega)}{\int_{E_g}^{\infty} P(\hbar\omega) d(\hbar\omega)}, \quad (4)$$

where  $\Delta G = 1.23$  eV represents the variation of the Gibbs free energy for water splitting. The effective energy required to drive the reaction accounts for the catalytic overpotentials of HER ( $\chi(\text{H}_2)$ ) and OER ( $\chi(\text{O}_2)$ ). The results obtained for the SMoSe|SeWS bilayer at pH=0 and the SeMoS|SWSe bilayer at pH=12.5 are sum-

marized in Table 3.

To ensure sufficient driving force, the overpotentials are typically compared against empirical benchmarks (0.2 eV for  $\text{H}_2$  and 0.6 eV for  $\text{O}_2$ ), leading to the following conditional form for  $E$ <sup>8,9,15,19</sup>:

$$E = \begin{cases} E_g, & \chi(\text{H}_2) \geq 0.2, \chi(\text{O}_2) \geq 0.6 \\ E_g + (0.2 - \chi(\text{H}_2)), & \chi(\text{H}_2) < 0.2, \chi(\text{O}_2) \geq 0.6 \\ E_g + (0.6 - \chi(\text{O}_2)), & \chi(\text{H}_2) \geq 0.2, \chi(\text{O}_2) < 0.6 \\ E_g + (0.2 - \chi(\text{H}_2)) + (0.6 - \chi(\text{O}_2)), & \chi(\text{H}_2) < 0.2, \chi(\text{O}_2) < 0.6 \end{cases} \quad (5)$$

For both configurations, the HER overpotentials are impressively low ( $\chi(\text{H}_2) = 0.08$  eV), while the OER ones remain well below the 0.6 eV. These minimal kinetic barriers ensure that a significant portion of the absorbed photon energy is effectively utilized to drive the redox reactions rather than being lost to overpotential requirements. Remarkably, both configurations yield an identical  $\eta_{\text{STH}} = 17.14\%$ , despite a difference in their band gaps of approximately 130 meV.

This similar efficiency is due to a direct trade-off between  $\eta_{\text{abs}}$  and  $\eta_{\text{cu}}$ . Specifically, SeMoS|SWSe has a higher  $\eta_{\text{abs}} = 65.39\%$  compared to SMoSe|SeWS, where  $\eta_{\text{abs}} = 58.24\%$ , because its smaller band gap allows it to harvest a broader range of the solar spectrum. However, this advantage is balanced by a lower  $\eta_{\text{cu}} = 26.22\%$ , compared to  $\eta_{\text{cu}} = 29.44\%$  predicted for SMoSe|SeWS. As a result, the relative increase in absorption for one configuration

Table 3 OER and HER overpotential ( $\chi(O_2)$  and  $\chi(H_2)$ , in eV), absorption efficiency ( $\eta_{abs}$ ), carrier utilization efficiency ( $\eta_{cu}$ ), and solar-to-hydrogen efficiency ( $\eta_{STH}$ ) calculated for SMoSe|SeWS at pH= 0 and for SeMoS|SWSe at pH= 12.5.

Configuration	$\chi(O_2)$	$\chi(H_2)$	$\eta_{abs}$ (%)	$\eta_{cu}$ (%)	$\eta_{STH}$ (%)
SMoSe SeWS	0.25	0.08	58.24	29.44	17.14
SeMoS SWSe	0.12	0.08	65.39	26.22	17.14

is compensated by a decrease in carrier utilization in the other, leading to nearly identical overall performance for both stacking orders. These calculated values are remarkably high, comfortably surpassing the 10% benchmark often cited for commercial viability<sup>8,12,48,49</sup> and highlighting a significant potential for the application of these Janus hetero-bilayers as efficient and sustainable photocatalysts for water splitting.

Additional tunability can be offered by strain (homogeneously distributed between both layers in all the considered heterostructures) which is known to substantially modulate the electronic and optical properties of both conventional and Janus TMDs.<sup>18,40,42,50,51</sup> Compressive and tensile strain shift the VBM and CBM, enabling control over band offsets and gap size. For example, in the SMoSe|SWSe bilayer, where the CBM lies slightly below the H<sub>2</sub> redox potential, suitable strain can widen the gap and align the band edges with the redox potentials required for overall water splitting, offering a promising direction for future research. As a final remark, it is important to note that under experimental conditions, ions can accumulate on the surfaces of these bilayers. Consequently, the photocatalytic performance may degrade, as the accumulated ions screen the internal electric field. Upon prolonged operation, this screening can lead to partial or even complete neutralization of the built-in field. Therefore, strategies to remove/redistribute these surface ions should be considered to maintain long-term performance by means of mechanical agitation or electrical perturbations such as the application of an external electric field.<sup>5,9</sup>

## Summary and Conclusions

In summary, we investigated from first principles the electronic and photocatalytic properties of Janus TMD hetero-bilayers. All considered systems are energetically stable, and their structural properties are primarily governed by the interfacial chalcogen atoms rather than the metallic species. Except for SeMoS|SeWS characterized by a direct band-gap at K, all other hetero-bilayers show indirect band gaps. Their energies are within the visible light range, making them suitable for solar energy harvesting. By calculating the intrinsic dipole moments and electrostatic potential profiles possessed by all these systems, we quantified the magnitude of the built-in polarization and connected it with the electronic structure of the systems. By evaluating band offsets relative to the HER and OER potentials, we found that the SMoSe|SeWS bilayer is the only heterostructure suitable for overall water splitting at pH= 0. On the other hand, SeMoS|SWSe exhibits favorable characteristics for overall splitting at alkaline conditions (pH $\geq$  12.5). In both cases, we found a remarkably high STH ef-

ficiency of 17.1%. Finally, the chemical potential difference between Mo and W, inherently present in the considered Janus TMD hetero-bilayers and generating an in-built electric field, ultimately promotes charge separation.

In conclusion, our findings demonstrate the potential of Janus TMD hetero-bilayers for photocatalytic water splitting. Their favorable level alignment, combined with their intrinsic polarization, not only makes them significantly more efficient photocatalysts than their homo-metal counterparts, but also paves the way to design new materials specifically tailored to this crucial application for sustainable energy production. The structural and chemical versatility of these heterostructures offers additional knobs to further optimize the catalytic performance, for example, via strain or through the controlled inclusion of defects, adsorbates, or heteroatoms. A systematic, high-level analysis of their optical properties is also needed to ultimately confirm their absorption efficiency across the visible spectrum.

## Acknowledgements

C.C. acknowledges funding from the German Research Foundation (DFG), project number 398816777, sub-project A8. M. T. and S. S. T. are grateful to support from Amirkabir University of Technology, Tehran, Iran.

## Author contributions

**Mostafa Torkashvand:** calculations and formal analysis, writing original draft; **Saeedeh Sarabadani Tafreshi:** review & editing; resources; **Surender Kumar:** conceptualization, validation, supervision, writing original draft; **Caterina Cocchi:** conceptualization, resources, supervision, writing – review & editing, project administration.

## Conflicts of interest

There are no conflicts of interest to declare.

## Data availability

Input and output files of the ab initio calculations performed in this work are available free of charge in Zenodo DOI: 10.5281/zenodo.18226319 [record:18226319].

## Notes and references

- 1 W.-J. Yin, H.-J. Tan, P.-J. Ding, B. Wen, X.-B. Li, G. Teobaldi and L.-M. Liu, *Mater. Adv.*, 2021, **2**, 7543–7558.
- 2 K. Maeda and K. Domen, *J. Phys. Chem. Lett.*, 2010, **1**, 2655–2661.
- 3 S. Nishioka, F. E. Osterloh, X. Wang, T. E. Mallouk and K. Maeda, *Nat. Rev. Methods Primers*, 2023, **3**, 42.
- 4 Z. Zou, J. Ye, K. Sayama and H. Arakawa, *Nature*, 2001, **414**, 625–627.
- 5 X. Li, Z. Li and J. Yang, *Phys. Rev. Lett.*, 2014, **112**, 018301.
- 6 C. Acar, I. Dincer and G. F. Naterer, *Int. J. Energy Res.*, 2016, **40**, 1449–1473.
- 7 X. Liu, P. Cheng, S. Li and W. Liu, *Adv. Mater. Interfaces*, 2023, **10**, 2300170.

8 L. Ju, M. Bie, X. Tang, J. Shang and L. Kou, *ACS Appl. Mater. Interfaces*, 2020, **12**, 29335–29343.

9 C.-F. Fu, J. Sun, Q. Luo, X. Li, W. Hu and J. Yang, *Nano Lett.*, 2018, **18**, 6312–6317.

10 X. Ye, F. Zhuang and R. Zhang, *Mater. Today Commun.*, 2023, **37**, 107351.

11 A. Rawat, M. K. Mohanta, N. Jena, Dimple, R. Ahammed and A. De Sarkar, *J. Phys. Chem. C*, 2020, **124**, 10385–10397.

12 N. T. G. Bao, T. N. Q. Trang, N. Thoai, T. B. Phan, V. T. H. Thu and N. Tuan Hung, *ACS Appl. Energy Mater.*, 2025, **8**, 5209–5221.

13 S. Wei, J. Li, X. Liao, H. Jin and Y. Wei, *J. Phys. Chem. C*, 2019, **123**, 22570–22577.

14 Y. Ji, M. Yang, H. Lin, T. Hou, L. Wang, Y. Li and S.-T. Lee, *J. Phys. Chem. C*, 2018, **122**, 3123–3129.

15 Z. Guan, S. Ni and S. Hu, *J. Phys. Chem. C*, 2018, **122**, 6209–6216.

16 L. Ju, M. Bie, J. Shang, X. Tang and L. Kou, *J. Phys. Mater.*, 2020, **3**, 022004.

17 X. Ma, X. Wu, H. Wang and Y. Wang, *J. Mater. Chem. A*, 2018, **6**, 2295–2301.

18 X. Xu, X. Jiang, Q. Gao, L. Yang, X. Sun, Z. Wang, D. Li, B. Cui and D. Liu, *Phys. Chem. Chem. Phys.*, 2022, **24**, 29882–29890.

19 C. Xia, W. Xiong, J. Du, T. Wang, Y. Peng and J. Li, *Phys. Rev. B*, 2018, **98**, 165424.

20 J. Zhang, S. Jia, I. Kholmanov, L. Dong, D. Er, W. Chen, H. Guo, Z. Jin, V. B. Shenoy, L. Shi and J. Lou, *ACS Nano*, 2017, **11**, 8192–8198.

21 A.-Y. Lu, H. Zhu, J. Xiao, C.-P. Chuu, Y. Han, M.-H. Chiu, C.-C. Cheng, C.-W. Yang, K.-H. Wei, Y. Yang, Y. Wang, D. Sokaras, D. Nordlund, P. Yang, D. A. Muller, M.-Y. Chou, X. Zhang and L.-J. Li, *Nat. Nanotechnol.*, 2017, **12**, 744–749.

22 S. Alfurhud, L. Saleem, A. Samad and U. Schwingenschlögl, *Solar RRL*, 2024, **8**, 2300992.

23 P. Hohenberg and W. Kohn, *Phys. Rev.*, 1964, **136**, B864–B871.

24 G. Kresse and J. Furthmüller, *Phys. Rev. B*, 1996, **54**, 11169–11186.

25 G. Kresse and D. Joubert, *Phys. Rev. B*, 1999, **59**, 1758–1775.

26 P. E. Blöchl, *Phys. Rev. B*, 1994, **50**, 17953.

27 J. P. Perdew, K. Burke and M. Ernzerhof, *Phys. Rev. Lett.*, 1996, **77**, 3865–3868.

28 J. Heyd, G. E. Scuseria and M. Ernzerhof, *J. Chem. Phys.*, 2003, **118**, 8207–8215.

29 J. Heyd and G. E. Scuseria, *J. Chem. Phys.*, 2004, **121**, 1187–1192.

30 S. Grimme, J. Antony, S. Ehrlich and H. Krieg, *J. Chem. Phys.*, 2010, **132**, 154104.

31 S. Grimme, S. Ehrlich and L. Goerigk, *J. Comput. Chem.*, 2011, **32**, 1456–1465.

32 V. Wang, N. Xu, J.-C. Liu, G. Tang and W.-T. Geng, *Comput. Phys. Commun.*, 2021, **267**, 108033.

33 C. E. Mørch Nielsen, F. Fischer, M. Prada and G. Bester, *2D Materials*, 2025, **12**, 045015.

34 J. C. Wildervanck and F. Jellinek, *Z. Anorg. Allg. Chem.*, 1964, **328**, 309–318.

35 R. Coehoorn, C. Haas, J. Dijkstra, C. J. F. Flipse, R. A. de Groot and A. Wold, *Phys. Rev. B*, 1987, **35**, 6195–6202.

36 K. E. Dungey, M. D. Curtis and J. E. Penner-Hahn, *Chem. Mater.*, 1998, **10**, 2152–2161.

37 W. S. Yun, S. W. Han, S. C. Hong, I. G. Kim and J. D. Lee, *Phys. Rev. B*, 2012, **85**, 033305.

38 C. E. Mørch Nielsen, F. Fischer and G. Bester, *npj 2D Mater. Appl.*, 2025, **9**, 11.

39 J. Chen, X. Zhao, S. J. R. Tan, H. Xu, B. Wu, B. Liu, D. Fu, W. Fu, D. Geng, Y. Liu, W. Liu, W. Tang, L. Li, W. Zhou, T. C. Sun and K. P. Loh, *J. Am. Chem. Soc.*, 2017, **139**, 1073–1076.

40 W. Guo, X. Ge, S. Sun, Y. Xie and X. Ye, *Phys. Chem. Chem. Phys.*, 2020, **22**, 4946–4956.

41 C.-H. Chang, X. Fan, S.-H. Lin and J.-L. Kuo, *Phys. Rev. B*, 2013, **88**, 195420.

42 S. Patel, U. Dey, N. P. Adhikari and A. Taraphder, *Phys. Rev. B*, 2022, **106**, 035125.

43 F. Li, W. Wei, P. Zhao, B. Huang and Y. Dai, *J. Phys. Chem. Lett.*, 2017, **8**, 5959–5965.

44 W.-J. Yin, B. Wen, G.-Z. Nie, X.-L. Wei and L.-M. Liu, *J. Mater. Chem. C*, 2018, **6**, 1693–1700.

45 J. M. Bolts and M. S. Wrighton, *J. Phys. Chem.*, 1976, **80**, 2641–2645.

46 T. A. Pham, D. Lee, E. Schwegler and G. Galli, *J. Am. Chem. Soc.*, 2014, **136**, 17071–17077.

47 X. Li, J. Yu, J. Low, Y. Fang, J. Xiao and X. Chen, *J. Mater. Chem. A*, 2015, **3**, 2485–2534.

48 C. R. Cox, J. Z. Lee, D. G. Nocera and T. Buonassisi, *Proc. Natl. Acad. Sci.*, 2014, **111**, 14057–14061.

49 M. Scharber, D. Mühlbacher, M. Koppe, P. Denk, C. Waldauf, A. Heeger and C. Brabec, *Adv. Mater.*, 2006, **18**, 789–794.

50 M. S. Ramzan and C. Cocchi, *Phys. Status Solidi RRL*, 2025, **19**, 2400276.

51 M. S. Ramzan and C. Cocchi, *Nanomaterials*, 2023, **13**, 2740.